Design and test of reliable high strength ingressive polycrystalline silicon microgripper arrays

Design and test of reliable high strength ingressive polycrystalline silicon microgripper arrays

S S Hazra[1,3], J L Beuth[1], G A Myers[2], F W DelRio[2] and M P de Boer[1]

[1] Mechanical Engineering Department, Carnegie Mellon University, Pittsburgh, PA 15213, USA
[2] Material Measurement Laboratory, National Institute of Standards and Technology, Gaithersburg, MD 20899, USA

E-mail: mpdebo@andrew.cmu.edu

Abstract

We present the design and validation of a micromachined gripper array that enables reliable transmission of forces of at least 14 mN. The gripper is constructed with polycrystalline silicon (polysilicon), a brittle material, and is compatible with polysilicon surface micromachining. Two ingressive snap-and-lock array designs are presented. After developing design guidelines, it is shown that the first gripper array is functional. However, a risk remains that the gripper array rather than the tensile bar that it grips in its intended application fails. Therefore, an improved geometry is designed and it is shown that it is robust with respect to failure. Scanning confocal Raman imaging directly confirms that the local peak tensile stresses in the robust gripper array are approximately 50% of the lower bound material strength, and also resolves a 25% stress variation across the array.

Keywords: microgripper array, snap-fit latch, MEMS reliability, confocal Raman stress imaging

(Some figures may appear in colour only in the online journal)

1. Introduction

Mechanical gripping of disjointed parts is a well-established area of study. A plethora of design strategies exist for linking mechanical objects on the macroscale [1]. The advent of micro- and nanomachining creates new opportunities for this art. Challenges include (1) identification of the design space as governed by the fabrication processes, (2) the effect of physical phenomena at this scale (e.g. small-scale materials and physics, adhesion and friction), and (3) attaining reliable operation.

Elegant and scalable micromanipulation solutions have been devised using microelectromechanical systems (MEMS) [2–11]. Most such solutions rely on the use of impactive gripper designs [2], i.e. 'tweezers', where the active mating pairs approach each other. The workpiece lies between the jaws of the gripper, which closes and opens. Such a design is applicable to wide-ranging tasks—from biological cell manipulation [3, 12, 13] to pick and place microassembly [5, 9, 13, 14]. The tweezers employ a variety of actuation mechanisms including piezoelectric [5], electrostatic [15], liquid bridge or electrowetting [16], electrothermal [6, 8, 17], and shape memory [18]. Even more elaborate designs including a microhand for gripping biological objects [7] and a multifingered drug-eluting device [11] have also been presented. A table summarizing tweezer sizes and workpiece volumes up to the year 2005 is given in [19]. Sizes range from a few hundred micrometers to several millimeters and workpiece volumes between tens of cubic micrometers to a cubic millimeter.

The design of microgrippers is guided by their intended use and the accessible fabrication process. Because samples to be manipulated are delicate, a high degree of force and

---

[3] Author to whom any correspondence should be addressed.
Present address: Ostendo Technologies, Carlsbad, CA 92011, USA
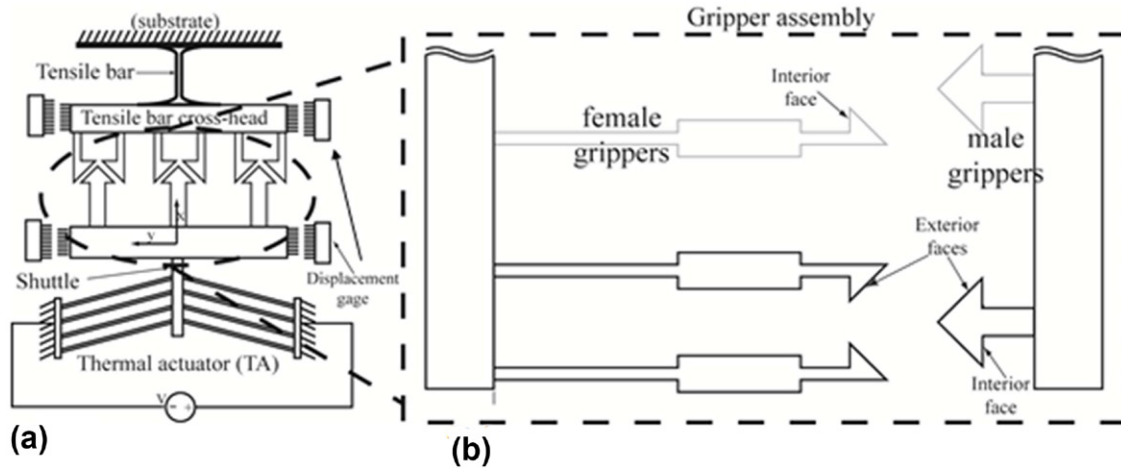
Figure 1. Detail of microgripper design. (*a*) Overall system with inset (*b*) showing part of the gripper assembly (rotated 90° CCW relative to (*a*)).

displacement control are required. Functional gripping [3, 6, 12, 19] and release [9] are the primary concerns, while gripper strength has not been an important issue. However, structural failure will become important when the microgrippers are subjected to significant stresses, especially when the constituent materials are brittle. This will occur if micromachined polycrystalline silicon (polysilicon), a widely used technical ceramic with a low fracture toughness of $1\,\mathrm{MPa\,m^{1/2}}$ [20], is used for gripping. Although brittle, the use of polysilicon in a gripping system is advantageous because it is already present in polysilicon-based microfabrication processes.

This paper presents the design of snap-and-lock [4] microgripper arrays of the ingressive type subject to high stresses. The basic design of the gripper is borrowed from the common macroscale solutions that exist for commercial snap-fit laptop lids, briefcase latches and printed circuit board zero insertion force (ZIF) terminals for flexible ribbons. We investigate two such designs for an on-chip polysilicon tensile tester [21]. With a lower bound strength of $2\,\mathrm{GPa}$ [22], the tensile bars are strong. Hence high forces are needed to break them and the associated stresses in the grippers are necessarily high. We detail the microgripper designs and show that each is functionally successful. However, only the improved design, in which the stress was reduced, resulted in high reliability. This work shows that highly reliable high load-bearing microgrippers can be designed with a brittle material.

2. Design overview of the tensile tester

Figure 1(*a*) shows the schematic layout of the on-chip polysilicon tensile tester. It is comprised of a chevron V-type thermal actuator (TA) [23, 24], a gripper system, a tensile sample and a displacement measurement system. The separately located actuator and tensile sample relieves residual stress, which can be significant in thin film materials [25], because the actuator and the test sample are initially separate. Testing requires mechanically connecting the actuator and sample using the microgrippers. While the overall design, operation

and strength results were reported [21, 26, 27], the gripper systems were not detailed, and are the focus of this paper.

In operation, current is passed through the TA legs, and the male grippers move forward due to Joule heating-induced expansion until the male and female gripper exterior faces, detailed in figure 1(*b*), come into contact. The male grippers then apply a bending moment to the female grippers which forces their spreading, allowing the male grippers to slide and snap-into the female grippers. This is described as the *insertion stage* of the operation.

The TA is now cooled by reducing the applied voltage, and the male grippers retract freely until their interior faces contact those of the female grippers. Further reduction in voltage effects a uniaxial stress across the tensile sample. This is described as the *retraction stage*. As can be noted in figure 1(*a*), tensile bar displacement is measured at the gages connected to the crosshead. The fracture strain can then be calculated by dividing the fracture displacement by the effective length of the tensile bar [21]. Knowing that polysilicon is a brittle material [20, 28, 29], and that the elastic modulus of polysilicon is $164.3 \pm 3.2\,\mathrm{GPa}$ [30], the fracture strength is calculated from the fracture strain value. Given that the strength ranges from 2.1 to $3\,\mathrm{GPa}$ for a $70\,\mu\mathrm{m}$ long tensile bar [27], the contribution of uncertainty in Young's modulus to the range in strength small.

The female grippers must be compliant in bending to ensure insertion. Upon retraction, they must be stiff axially, which enables a large force to be transmitted. Because they potentially can fracture instead of the specimen, it is important to consider the grippers' load-bearing ability in detail.

Figure 2 shows a schematic load–displacement diagram for the tensile tester. This diagram is explained in detail in [21], and is briefly described here. The insertion stage is in the upper quadrant while the loading stage is in the lower quadrant. Using a numerical framework for TA design as presented in [23, 24], we can calculate the maximum displacement $x_{\max}$ and the maximum compressive force the TA can sustain during insertion (line 1 in figure 2).

The shuttle and male grippers are rigidly connected as each consists of three laminated layers of polysilicon, and their
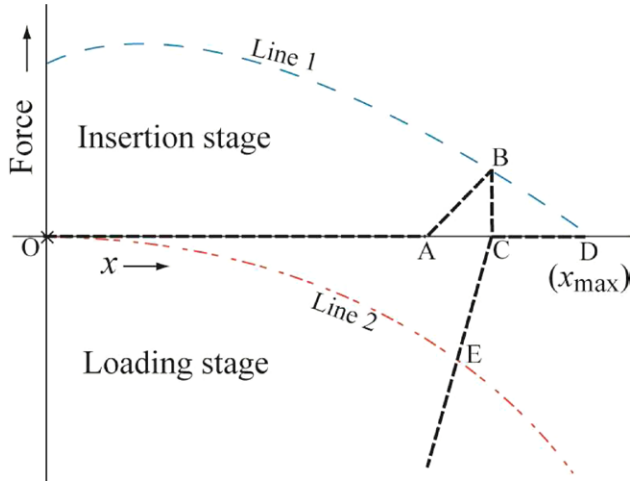
Figure 2. Schematic load–displacement diagram of the microtensile test system.

displacement is represented by x in figure 2. During insertion, the male grippers move freely from point O to A. At point A the male gripper exterior faces come in contact with female gripper exterior faces and the TA develops an insertion load. The slope of the line AB is due to the in-plane bending stiffness of the female grippers. At point B, the male grippers insert completely into the female grippers and the load drops back to zero at C. As the TA legs are heated further, displacement continues to point D. This completes the insertion stage.

During retraction, the male grippers travel back, and the interior faces of the male and female grippers come into contact at C. Upon further cooling, the TA applies a tensile load across the sample and fracture takes place along the load line from C to E, whose slope represents the combined axial stiffness of the gripper and the tensile specimen system. The primary function of the grippers in this stage is to transfer the axial stress applied by the TA to the tensile specimen without failing or stretching.

The important design guidelines for the tensile tester are:

(a) to keep the ordinate of point B under or on line 1 (to allow insertion);
(b) to minimize the distance CD (extra travel beyond point C reduces the maximum force obtainable from the TA);
(c) to maximize OD and the ordinate of point E (to maximize the force available to fracture the tensile bar).

Point A can be ascertained as follows: the slope of the line AB is determined by the in-plane bending stiffness of female grippers. The distance AC is fixed by the geometry of the gripper heads. Points C and B have the same abscissa; the ordinate of point B is known from the slope of AB. According to design guideline (2), the distance CD shall be minimized. This is achieved if point B lies exactly on line 1. Consequently, the absolute position of ΔABC with respect to point O are fixed.

3. Microgripper array design and test

This section describes the design principles considered for two gripper arrays, followed by experimental observations.

We call the first and second designs the 'simple' and 'robust' designs, respectively. Figure 3 presents the coordinate system. Figures 4(*a*) and (*b*) present a schematic representation of simple female and male grippers respectively along with their design geometry.

3.1. Insertion, retraction and loading considerations

3.1.1. Insertion—calculating distance AC. Let us reference x_c (figure 4(*b*)) to point A (figure 2). When $x_c = 0$, the male grippers first make contact with the female grippers. We require the value of x_c at point C, where insertion occurs. From figure 4(*b*) it can be seen that the distance the male grippers must travel is proportional to the overlap between the male/female gripper heads, or,

$$AC = o \tan \theta. \tag{1}$$

At insertion, $x_c = AC$. The female grippers will separate from an initial gap of $\delta_A = S_f - 2w_2$ to $\delta_C = 2b + w_m$. Just before insertion, $2\delta = \delta_C - \delta_A = w_m + 2b + 2w_2 - S_f$, where δ is the deflection of each female gripper tip. During insertion, δ can be related to x_c as

$$\delta = x_c \left(\frac{w_m + 2b + 2w_2 - S_f}{2o \tan \theta} \right). \tag{2}$$

3.1.2. Insertion—slope of line AB and force at point B. Let us consider the free body diagram of a male–female gripper head as shown in figure 5. Let F_a be the force applied on a single male gripper by the TA. This force causes the male grippers to slide across the female gripper face. We assume that the reaction forces between the contacting faces are the normal force F_N and the friction force, equal to $F_f = \mu F_N$, where μ is the coefficient of friction. The components of these forces result in the bending force, F_b, and the compressive force, F_c, on the female grippers. From statics,

$$\frac{F_a}{2} = F_c = F_N \left(\mu \sin \theta + \cos \theta \right), \tag{3a}$$

and

$$F_b = F_N \left(\sin \theta - \mu \cos \theta \right). \tag{3b}$$

Assuming $L_f \gg (d_f + h_f)$, the bending force required to bend a single female gripper by a distance δ can be estimated from linear elasticity as

$$F_b = \frac{3EI_f}{L_f^3} \delta = \frac{3Et_f w_f^3}{12L_f^3} \delta = \left(\frac{w_m + 2b + 2w_2 - S_f}{o \tan \theta} \right) \frac{Et_f w_f^3}{8L_f^3} x_c$$
$$= F_b(x_c). \tag{4}$$

Here t is the thickness (out-of-plane) of the features in figures 3–5. Using equations (3b) and (4), we can express F_N in terms of x_c as

$$F_N = \frac{1}{(\sin \theta - \mu \cos \theta)} \left(\frac{w_m + 2b + 2w_2 - S_f}{o \tan \theta} \right) \frac{Et_f w_f^3}{8L_f^3} x_c. \tag{5}$$

Finally, we can write F_a in terms of x_c using equations (5) and (3a) as
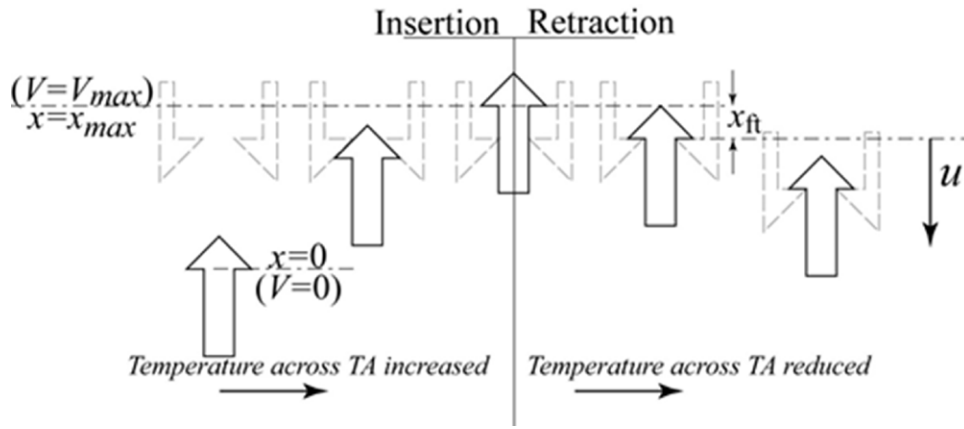
Figure 3. Chip-referenced coordinate system used in describing male gripper/TA shuttle travel with respect to female grippers/μTB.
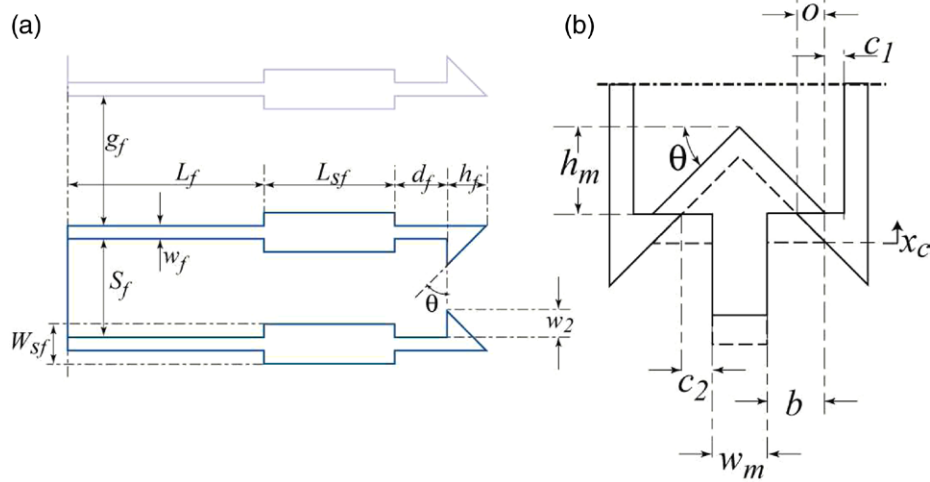
Figure 4. Gripper design term definitions with the (*a*) female grippers and (*b*) male grippers.
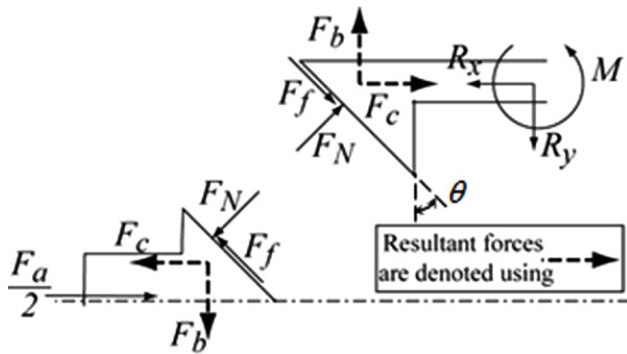
Figure 5. Free body diagram of male–female gripper interaction during insertion.

$$F_a = \frac{(\mu \sin \theta + \cos \theta)}{(\sin \theta - \mu \cos \theta)} \left(\frac{w_m + 2b + 2w_2 - S_f}{o \tan \theta} \right) \frac{E t_f w_f^3}{4 L_f^3} x_c. \quad (6)$$

As we have three structural layers in our design and N_g male grippers per layer, the total force applied by the TA to complete insertion is

$$F_{\mathrm{TA}} = \frac{3 N_g \, E t \, w_f^3}{4 L_f^3} \frac{(\mu \sin \theta + \cos \theta)}{(\sin \theta - \mu \cos \theta)} \left(\frac{w_m + 2b + 2w_2 - S_f}{o \tan \theta} \right) x_c. \quad (7)$$

The value of x_c at point B in figure 2 is $o \tan \theta$. So the magnitude of the compressive force acting on the TA at point B is

$$F_{\mathrm{TA}} \bigg|_B = \frac{3 N_g E t w_f^3}{4 L_f^3} \frac{(\mu \sin \theta + \cos \theta)}{(\sin \theta - \mu \cos \theta)} \left(w_m + 2b + 2w_2 - S_f \right). \quad (8)$$

The above equation helps determine the location of point B and ΔABC in figure 2. However, due to unknown local variations in surface micromachining process tolerances and friction values, it is risky to assume that insertion takes place uniformly across all the gripper exterior faces. This means that $F_{\mathrm{TA}}|_B$ could exceed the values prescribed by line 1. Therefore, we shift the point C to the left by a distance we call *free travel*, x_{ft}, as indicated in figure 3. A value of $x_{\mathrm{ft}} = 0.5\,\mu$m was empirically chosen to ensure a high likelihood of complete insertion. Hence $OC \approx OD - x_{\mathrm{ft}}$. The value of x_{ft} is kept small relative to OD following tensile tester guideline (2). However, values of x_{ft} that are too small may not enable complete insertion of the male gripper array into the female array. In the practical implementation, $F_{\mathrm{TA}}|_B$ is small, i.e. the ordinate of B is substantially below line 1, which results in $OA + AB \approx OC$.

Let us note that the direction of F_b from equation (3b) depends on the sign of $(\sin \theta - \mu \cos \theta)$. So for $\mu > \tan \theta$, we get bending in the opposite direction to the one considered
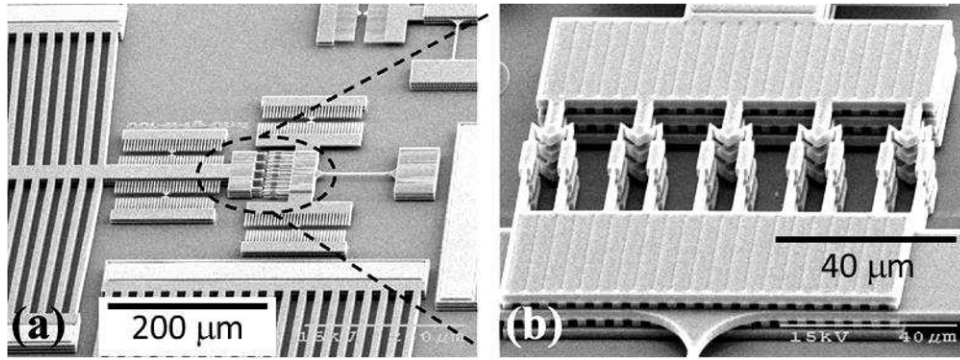
Figure 6. (*a*) Fabricated tensile tester. (*b*) The simple gripper system after engagement. The three layers of structural polysilicon can be observed.

in the free body diagram given in figure 5. Also, if $\mu = \tan\theta$, the female gripper legs may buckle. With $\theta = 45°$, this $\mu < 1$ is required for insertion.

3.1.3. Retraction and loading.
In the retraction stage, the grippers travel freely from point *D* to point *C*. At *C*, the male grippers come in contact with the female grippers and apply tensile load to the sample. This results in a stretching of both the grippers and the sample. Assuming perfect contact (i.e. ignoring asperities on the contacting surfaces), the load–displacement behavior is linear and the slope of the line CE can be estimated by assuming the tensile bar and the narrow sections of the grippers are simple elastic beams in tension. This is detailed in [21].

The maximum load that a given design can apply to the sample is the load applied after the TA has been cooled to ambient temperature. Figure 2 shows the corresponding load line (line 2), as determined by finite element analysis (FEA) [21]. From section 3.1.2 we know the position of point *C*. The maximum force applied by the TA can thus be computed to be the intersection of line 2 with the load line *CE* for the tensile sample.

3.1.4. TA design.
TA design is governed by the force it can generate (proportional to stiffness of the TA), its travel (proportional to TA leg length), the nominal stiffness of the microtensile bar and the estimated fracture strength of the sample material. A numerical model can be used to obtain a good approximation of the TA voltage–thermal–structural deflection behavior and the maximum compressive load the TA can sustain as has been detailed in [21, 23, 24]. As shown in figure 2, this gives the value of x_{max} (8 μm at $V_{max} = 6.4$ V) and establishes the placement of the female gripper array after choosing the value of x_{ft}, the free travel.

3.1.5. Simple gripper design.
Figure 6(*a*) shows a scanning electron micrograph of the fabricated microtensile test system, while figure 6(*b*) shows a close-up of the simple gripper array. The three main structural levels of polysilicon, Poly 12, Poly 3 and Poly 4, in the SUMMiT V process [31] are connected vertically in order to maximize its axial stiffness and its resistance to buckling.

Table 1. Parameter values selected for simple grippers (figure 4).

Parameter	Value
Male grippers (15 total)	
b	2 μm
w_m	3.5 μm
h_m	3.5 μm
Female grippers (15 pairs)	
g_f	10 μm
S_f	7.5 μm
w_f	1 μm
w_2	2 μm
W_{sf}	3 μm
L_{sf}	10 μm
L_f	15 μm
d_f	4 μm
Common to male and female grippers	
N_g	5
# of gripper layers	3
o	2 μm
c_1	0 μm
c_2	0 μm
θ	45°
t[a]	2.25 μm

[a] $t = 2.25$ μm for top two structural layers and 2.5 μm for bottom structural layer.

The values of simple gripper parameters (figure 4) are given in table 1. Key selections are discussed in this section. Many other parameters are involved in the gripper design, and interact with other performance measures and are described in [21, 32].

The rectangular features of length L_{sf} in figure 4(*a*) are the location where the layers are connected vertically by sacrificial oxide cuts on the female grippers. They can be identified in figure 6(*b*). The rectangles must be positioned so that they do not interfere with the male gripper heads during insertion.

The distance x_c is determined by the geometry of the gripper heads. The female gripper head (a right isosceles triangle with the hypotenuse as the active mating face during insertion) has lengths of $h_f = 3$ μm for the equal sides, and the male gripper head, with $h_m = 3$ μm combines two such triangles. This geometry establishes the maximum stress at the base of the female grippers during insertion, and also controls
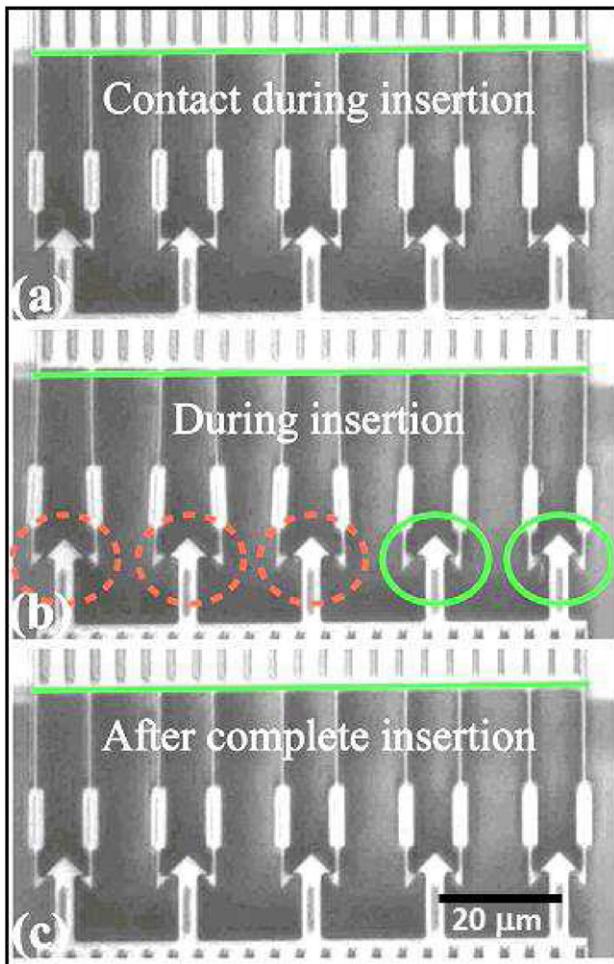
Figure 7. Optical images of insertion process indicating μTB crosshead rotation. (*a*) The male–female grippers in contact during the initial stages of insertion. (*b*) Two male grippers (on far right, outlined with solid ovals) completely inserted, with the remaining three grippers (outlined by dashed ovals) on the left still in the process of inserting. The small angle made with the horizontal green solid line with the crosshead depicts crosshead rotation. (*c*) Shows that all the grippers have fully inserted.

the overlap and hence the normal stress transferred across the gripper parallel faces during the retraction process.

An important issue is that female gripper bending stiffness must be low during insertion, but axial stiffness must be high during retraction. The ideal value of N_g is not immediately clear. A design using a single gripper pair could have been chosen. To sustain high axial stiffness during retraction, it would require a wide female member. This in turn would lead to high bending stiffness, and could lead to buckling in the TA legs during insertion. To avoid this, we chose to use a uniform array of slender gripper pairs that are compliant with respect to in-plane bending. The minimum linewidth of the micromachining process [31] limits the slenderness of the grippers and the feature size of the gripper head design. The length and width of each of the female grippers (not including the head or sacox cuts) was set at $L_f = 15\,\mu$m and $w_f = 1\,\mu$m respectively, and a length of $10\,\mu$m and $w_m = 3.5\,\mu$m for the male grippers. The effective axial stiffness of the combined gripper system is calculated to be about 25 times that of the tensile bar. Also, the
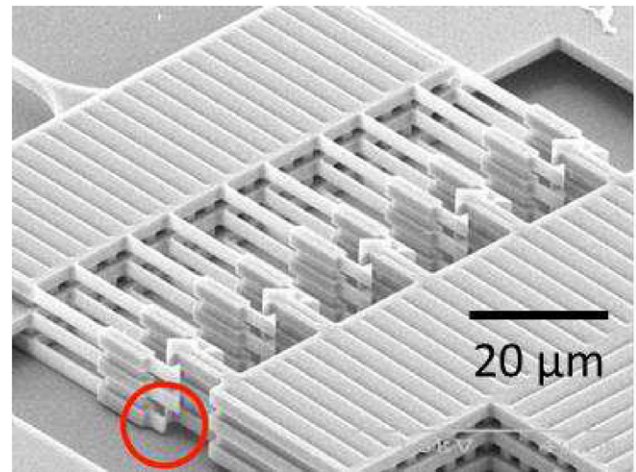
Figure 8. Fractured simple gripper specimen with a broken head (encircled). The fracture occurred at the corner of the interior face.

total female gripper cross-section leads to axial stresses that are lower by a factor of 15 than the axial stress in the tensile bar. We discuss the experimental effect of N_g in section 4.3.

The effective area supporting the applied tensile load is 15 times less than that on the tensile bar. Therefore, concentrated stresses in the grippers were presumed to be small compared to stress in the tensile bar. Overall, the grippers discussed in this article are approximately 10 to 50 times smaller compared to previous work [4, 33].

3.2. Simple gripper experimental results

During insertion, initial contact across the gripper array was usually observed to be uniform, but inevitably a gripper pair on one side of the array completed insertion before the other. This induced a noticeable rotation of the tensile bar crosshead, which may have resulted from a variation in frictional resistance or micromachining process inhomogeneities between gripper pair faces. This observation highlighted the importance of the free-travel design parameter, $x_{ft}>0$, which enabled the male grippers to insert even if the crosshead rotated during experiments. The optical images presented in figure 7 (using a 50 × Mitutoyo objective with NA = 0.55), show rotation between the solid green line and the female gripper bases at the crosshead (figure 7(*b*)). After complete insertion, the male members were no longer in contact with the females, and the original alignment of the μTB is elastically restored (as shown in figure 7(*c*)).

The experimentally obtained displacement-to-fracture measurements during retraction have been described in detail [21, 26]. Here, we focused on post-experiment gripper examination under a scanning electron microscope (SEM). As shown in figure 8, this revealed a pair of broken female gripper heads (out of 15 such pairs). Because of the brittle nature of the fracture process, which involves short fracture times, it was unclear if the heads broke during loading, thereby initiating the fracture event, or after fracture of the tensile bar which involved significant energy release. This question could be addressed indirectly. The simplest method was to collect
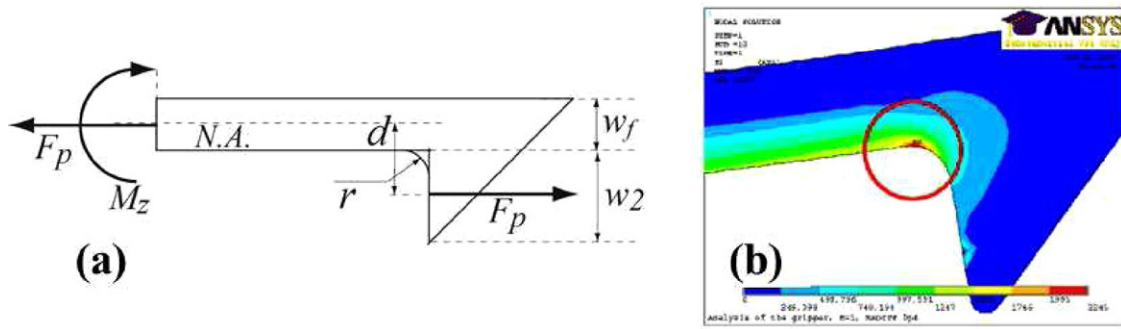
Figure 9. (*a*) Free body diagram of the female gripper head illustrating the single-point contact assumption and its location. (*b*) Finite element simulations predict the location and magnitude of concentrated stresses in a female gripper head with simple design.

measurements and examine the data for the presence of distinct and separated populations, which would indicate the presence of distinguishable modes of failure. Weibull test data [21, 26] measured using the simple gripper design, did not show any such distinguishing features. Moreover, the presented failure strength measurements corresponded with values presented in often-referenced literature [34, 35]. This lead to an initial conclusion that failure occurred in the tensile bars.

A second method for addressing the first-to-fail question was to determine the loads at which the simple grippers failed in the absence of the tensile bar. If these loads were higher than the loads required for the designs with tensile bar to fail, then we might assume the tensile bar always failed first. To this end, we co-fabricated a device that lacked a tensile bar such that the male grippers would apply stresses only to the female gripper system. We constructed a force–displacement plot for the with-tensile bar and without-tensile bar systems (as shown in figure 9 in [21]) to extract the loads at which the components fail. We found that both the with-tensile bar device and the without-tensile bar device failed at approximately the same applied load (9 mN). Hence, the load required to fracture grippers was approximately the same as the load required to fracture the tensile bar.

A common feature to most damaged grippers (based on 10 post-failure crossheads examined) was that the damage was sustained only at the female gripper heads with the fracture locations about the re-entrant corner of radius r as shown in figure 9(*a*). Evidently on the damaged gripper heads, the $r \approx 0.4\,\mu$m was not large enough to reduce stresses caused either during testing or collision afterwards. The measured load at which the female grippers in the without-tensile bar design failed was used to calculate the magnitude of concentrated stresses in this region at failure. As discussed in the next section, we found that the amplified stresses were of the same order as the stresses acting in the tensile bar cross-section. It can be argued that the magnified stresses act only in a very small volume in the female grippers. Therefore, the probability of existence of fracture initiating defects within that small volume is also low (especially when compared with the tensile bar). Hence the small volume should have exhibited higher strength. Most likely, the tensile bar failed first in the experiments. Nonetheless, female gripper failure prior to tensile sample failure in the simple gripper design could not be ruled out. Therefore, an improved design was sought.

4. Robust gripper design

We presented a simple gripper design based on simple strength of materials concepts in the previous section. It yielded complete operational functionality: it inserted, retracted and applied tensile loads as desired and the resulting data agreed with established literature. The design was based on the *a priori* assumption that surface micromachining induced radius of curvatures at sharp corners would be sufficient to remove stress concentration effects. In this section, we present a 'robust' gripper design with a larger radius of curvature at re-entrant corners.

4.1. Stress concentration analysis

We first estimated the amplified stresses in the simple gripper head corner with analytical calculations. We used this amplified stress magnitude as a comparative metric in identifying the robust geometry that significantly reduces the stress amplification factor. Figure 9(*a*) shows a free body diagram of the female gripper head. F_p is the load applied on each female gripper head by the TA during retraction. Assuming that the tensile load is uniformly distributed over the female gripper array, we can determine the magnitude of F_p using the load value at which the female grippers in the no-tensile bar design fractured, as discussed in the previous section. A load of $F_p = 10\,\text{mN}/(3 \times 2 \times N_g) = 0.33\,\text{mN}$ is assumed to transfer through a point contact between the male–female grippers at distance of $(w_f + w_2)/2$ from the neutral axis of the gripper beam. The re-entrant corner, with radius of curvature r, experiences normal and bending stresses; these are amplified by axial and bending stress concentration factors of k_a and k_b respectively. Denoting the normal stress by σ_a and the bending stress by σ_b, the amplified stress σ_{xx} acting in the corner is

$$\sigma_{xx} = k_a\sigma_a + k_b\sigma_b = k_a\frac{F_p}{w_2 t} + k_b\frac{F_p\left(w_f/2\right)\left(w_2 + w_f\right)}{2I_{xx}}$$

$$= k_a\frac{F_p}{w_2 t} + k_b\frac{3F_p\left(w_2 + w_f\right)}{w_f^2 t} \ . \tag{9}$$

The stress amplification factors were estimated from similar geometries presented in [36] and depend upon the exact values of w_2 and w_f. Equation (9) was used to compute the amplified stresses as a function of the geometry of the female gripper head analytically.

Table 2. Parameter variation and maximum stress values for robust gripper with $w_2 = 2\,\mu$m.

Case	w_f (μm)	r (μm)	Analytical stress (GPa)	Numerical stress (from FEA) (GPa)
1[a]	1	0.4	2.48	2.25
2	1	1.0	2.01	1.76
3	2	0.4	0.87	1.02
4[b]	2	1.0	0.86	0.74

[a] Used in simple gripper design.
[b] Used in robust gripper design.
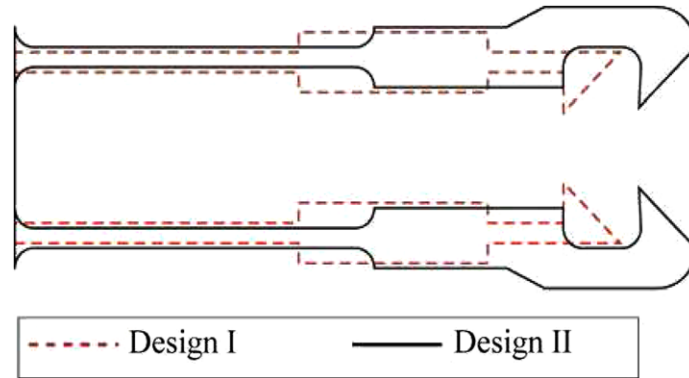
Figure 10. Simple female gripper design (red dashed line, design I) and robust gripper design (black solid line, design II).

The magnitudes of k_a and k_b were obtained from approximations of the actual design. FEA provides a better estimates of these values. Figure 9(*b*) shows the stress concentration about the re-entrant corner in the simple gripper design as obtained from ANSYS. A plane82 element under plane stress condition was chosen to model the structure.

The robust design relies primarily on larger corner curvature and a wider female gripper head compared to the simple gripper design. For the robust design, we consider four design cases in which w_f and r are varied.

The equivalent stress values at the corner for the four design variations are provided in table 2, column 5. These stress values were checked for convergence with increasing mesh resolutions to ensure the accuracy of the finite element calculations. The ratios of finite element values for different designs were compared with ratios of analytically calculated values using equation (12) (table 2, column 4) to check the validity of the FEA model and were found to be consistent.

The normal stress acting on the tensile bar is equal to $(10\,\text{mN}/2.25 \times 2\,\mu\text{m}^2 = 2.22\,\text{GPa})$. As noted in the last section, this value is close to the magnitude of amplified stress in the simple gripper head at 2.25 GPa (case 1 in table 2). Since the geometrical parameters for case 4 in table 2 reduced the amplified stress magnitude by ≈ 3 times, they were selected for the robust gripper design. The robust design is shown in figure 10 (solid outline), with the simple design shown (dashed) for comparison. It can be noted that the bending stress during insertion acting on the robust female grippers does not change significantly.

4.2. Robust gripper experiments

In experiments on devices with robust gripper arrays *without* tensile bars (shown in inset of figure 11(*a*)), no gripper failure was observed even after the TA was cooled down to room temperature. Figure 11(*a*) shows the measured displacement in a no-tensile sample device as the TA is being cooled with (i) a robust gripper array (circles) and (ii) a simple gripper array (solid). It illustrates that though the simple grippers are not able to sustain TA loads under 3 V, the robust grippers do not fail even after the female grippers are stretched by about 250 nm, corresponding to a force of 14 mN. This can be compared to a force of 9 mN at which these simple grippers without tensile bar fractured [21].

SEM imaging of 34 devices with the robust gripper design and *with* tensile bars also indicated no gripper failure. An intact robust female gripper array *after* tensile bar fracture is shown in figure 11(*b*).

4.3. Comparison of 5 gripper pairs to 3 and 7 gripper pairs

So far, in all testing reported, $N_g = 5$. Here, we compare simple and robust gripper designs with varying N_g. The different designs are listed in table 3, with sets A–C corresponding to simple grippers of 3, 5 and 7 pairs, and sets D–F robust grippers also with 3, 5 and 7 pairs. Although some rotation was observed, *insertion* of sets B and E (5 pairs) always took place at a predictable voltage value for both simple and robust designs. However, with sets A and D (3 pairs) and sets C and F (7 pairs), insertion was not predictable. For these sets, cycling of the TA voltage was required until all grippers engaged; this process was manual and time consuming. Additionally, female gripper heads were sometimes damaged during insertion. With sets A and D (3 pairs), the main problem was larger crosshead rotation, and with set A the rotation was large enough that female grippers sometimes broke at their base. With sets C and F (7 pairs), the main problem was non-uniform insertion
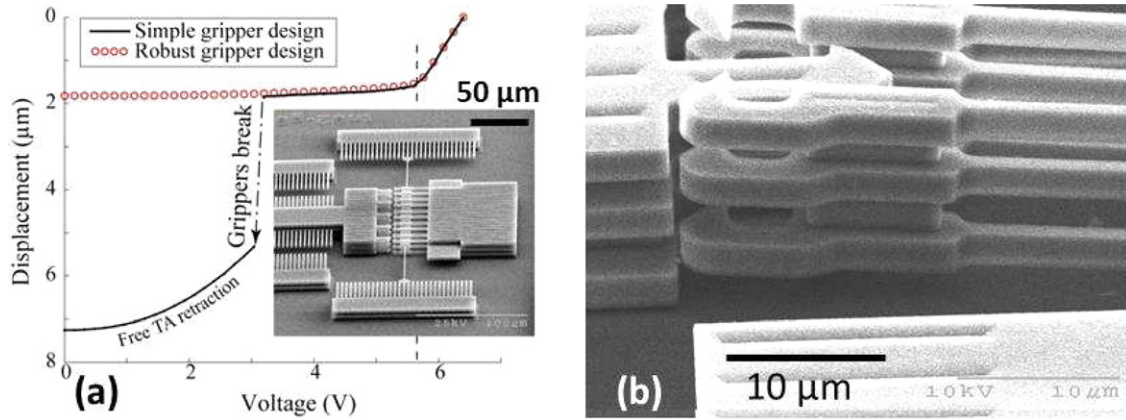
Figure 11. (*a*) Voltage–displacement plot from devices without tensile bar (shown in inset). Displacements from the robust gripper design are shown using circles. Displacements from the simple gripper design are shown with the solid line. (*b*) An example robust gripper design *after* a tensile bar has been fractured. No gripper head failures can be detected.

Table 3. Comparison of 3, 5 and 7 gripper pair designs.

Set	Gripper design	N_g	N (# tested)	$\overline{\sigma}_f$ (GPa)	σ_f std dev (GPa)	Comments
A	Simple	3	10	1.69	0.18	Rotation during insertion, noisy retraction curves
B	Simple	5	34	2.35	0.24	Predictable insertion voltage, smooth retraction curves, intermittent gripper failure suspected during retraction
C	Simple	7	9	2.53	0.13	Rotation during insertion, manual insertion required, noisy retraction curves
D	Robust	3	7	2.41	0.31	Rotation during insertion, manual insertion required, smooth retraction curves
E	Robust	5	231	2.55	0.17	Predictable insertion voltage, smooth retraction curves, no gripper failure observed
F	Robust	7	7	2.51	0.27	Rotation during insertion, manual insertion required, smooth retraction curves

(some would insert but others would not), however, gripper failure was not observed.

For sets A and C (simple), during *retraction* the displacement versus TA voltage data was noisy. Comparatively, the sets B (simple) and D–F (robust) retraction measurements were generally smooth. The displacement noise may be correlated with female gripper fracture or at least rearrangement of the gripper heads. In particular, for set A there were often observable female gripper head failures, and also the mean strength $\overline{\sigma}_f$ of 1.69 GPa was significantly lower as compared to sets D–F of ≈2.5 GPa (see table 3). Sometimes in set A all grippers failed and the tensile bars did not break—strength (σ_f) measurements reflected only those events in which the tensile bar fracture clearly could be identified. It is also seen that $\overline{\sigma}_f$ for set B is slightly lower than sets C and D–F. The data set B was reported in [21], while the data from set E was reported in [27].

Figure 12 shows boxplots of the strength data from set A–F. Outliers at 1.8 GPa and 2.0 GPa can be noted in sets D and F, respectively. They were attributed to the insertion problems just described. For set E, only 50 data points (randomly selected) are shown in order to make a comparison in the data range with respect to set B (34 data points). Keeping in mind that nominally the same tensile bars are being tested, it is apparent from figure 12 that set A (3 pairs) has lower average strength than the other sets. This reflects the observation that

grippers often failed in set A. It is also apparent that set B tends to have more low strength values than set E. This is apparently due to the difficult-to-detect gripper failures in set B.

A simple statistical test confirms these differences. Let us consider the confidence that the mean of a given set is different from the mean of set E (for which there were no gripper failures). According to a student's *t*-test, confidence is greater than 99.99% that the means of sets A and B are each less than the mean of E. For the other data sets (C, D and E), the confidence levels are low (<90%).

4.4. Direct validation of robust female gripper stresses by confocal Raman

It is useful to validate the actual stress levels in the female grippers. In a previous report [37], varying numbers of the TA leg pairs were broken *before* insertion. Then upon retraction, a large, variable static stress remained after the voltage across the TA legs was reduced to zero and the tensile bar and gripper assembly remain loaded. It was shown that the stress distributions in the tensile bar could be imaged with high fidelity using confocal scanning Raman microscopy. The Raman microscope details are described in [37]. Here we use the same technique to evaluate the stress levels in a strained robust gripper assembly. After loading with eight intact TA leg pairs, corresponding to 8 mN total force, the top array of
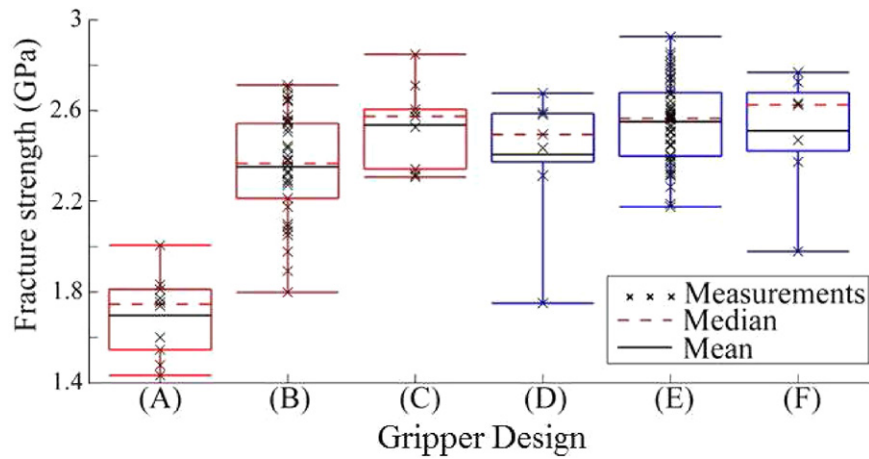
Figure 12. Boxplots of the strength data from gripper designs A–F as described in table 3.
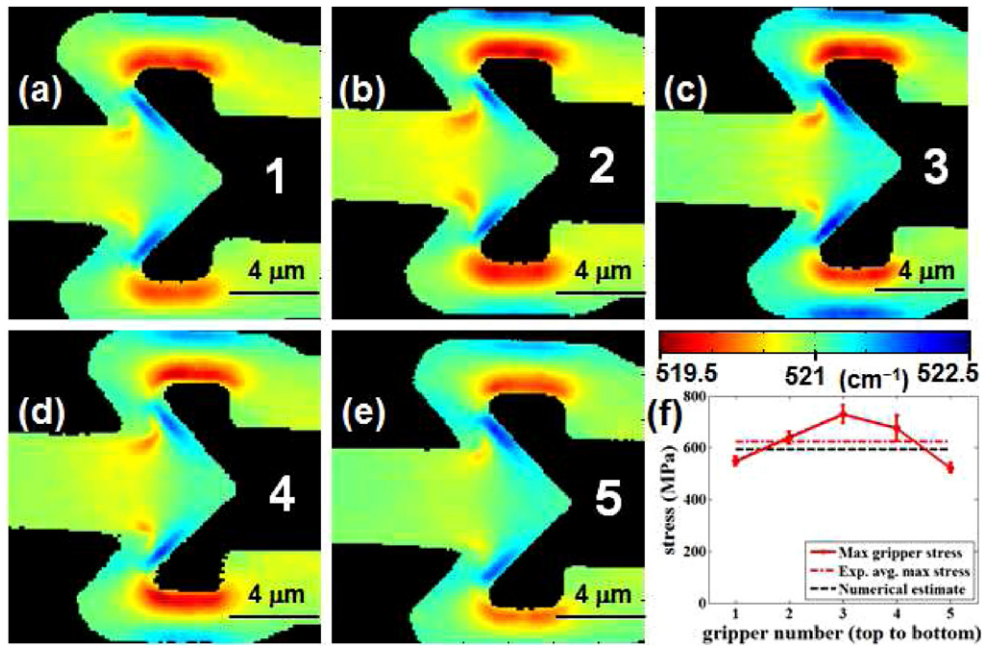
Figure 13. Raman maps of statically loaded topmost female/male gripper pairs with $N_g = 5$. Scale bar indicates Raman shift spectral peak positions. Red indicates highest tensile stress while blue is compressive. (*a*)–(*e*) Individual gripper pairs. (*f*) Maximum tensile stress in each gripper pair (error bars indicate ± one standard deviation), compared with numerical estimate.

gripper pairs were imaged with the same confocal scanning Raman instrument, here with a diffraction-limited lateral resolution of $0.20\,\mu$m. Regions of tension and compression are well distinguished, as seen in figures 13(*a*)–(*e*).

The local maximum stresses in the female grippers were estimated as follows. First, the cross-sectional area of the male grippers is $160\,\mu$m^2, giving rise to a tensile uniaxial stress of 50 MPa (green region on left of figures 13(*a*)–(*e*)). The conversion factor from Raman wavenumber to stress is c_f $= -522.5\,$MPa/cm^{-1} (note $c_f < 0$) for the current system [37]. The ten highest wavenumbers (*hwn*) of pixels in the uniaxially loaded male gripper region (green) were then subtracted from the ten lowest wave numbers (*lwn*) in the female gripper region (red), and multiplied by c_f. This was done for both the

upper and lower half of each female gripper. Finally, the stress was calculated from

$$\sigma = 50\ \text{MPa} + c_f\,(lwn - hwn)\,, \qquad (10)$$

and the standard deviation of (*lwn* –*hwn*) was also obtained to estimate variation within a given female gripper pair. The results are plotted in figure 13(*f*). It is seen that the average stress agrees well with the numerically estimated stress (reduced from the value in table 3 because the load with 8 legs is 8 mN). Furthermore, the stress is greatest in the central gripper pair. This can be attributed to a small degree of in-plane bending compliance of the crosshead. The maximum stress value in the female grippers is ≈700 MPa, which would become ≈900 MPa if loaded to 10 mN. This is well below the

threshold strength of the material, ≈2 GPa [27]. In contrast, the estimated simple female gripper stress of 2.5 GPa (table 3) exceeds the threshold strength.

5. Discussion

Due to the problems associated with observation and inspection in MEMS, we find that basic test system functionality does not ensure reliable statistical strength data gathering. Taken together, the data of table 3, especially sets A and B, indicate the problem with the simple gripper design. However, the robust microgripper array E does sustain the large loads without contributing artifacts to the tensile strength measurements of polysilicon. Indeed, this design was used for 231 strength measurements to derive three-parameter Weibull values, which included a threshold strength of 2.08 GPa [27].

A distinct advantage of the SUMMiT V process is that it has four independent structural levels [31]. To maximize the bending and minimize the axial compliances, the arrays designed here were in three polysilicon levels connected by sacox cuts. More often, micromachining processes have fewer structural levels. It would be useful to demonstrate a single level of robust grippers for high load applications.

We rely on interfaces to guide motion and transmit loads. While more analysis would be necessary to understand in detail why the five gripper pairs inserted the most uniformly, we can consider the possible underlying reasons. These may be associated with fabrication process tolerances and linewidth uncertainties, or more likely with surface effects such as friction. This is illustrated in table 3 with respect to N_g variations. When we change the number of gripper pairs, we modify the interface area over which interaction can take place. Though the SUMMiT V process results in fairly smooth surfaces (~10 nm root mean square sidewall roughness [27]), polysilicon tribological behavior is, in general, not tightly predictable [38]. Increasing the gripper pairs results in an increase in the interaction area, while decreasing the possibility of stress singularities, and vice versa. Hence, a greater number of interfaces results in increasing the uncertainty in the system. We see this in the insertion characteristics of the 7-pair robust gripper design. But when we reduce the interaction area, we start increasing the likelihood that stress singularities induce fracture. This is what we observe in the 3-pair robust gripper tests. We can also note that the derivations in section 3 assumed that μ is a constant. If it varies from one gripper to another, the analysis becomes considerably more complex.

The 5-pair robust microgripper array design presented here successfully miniaturize the common latches found on the macroscale. It is easy to visualize a multitude of microlatching applications fabricated using this design, for example snap-fit wire-bond terminals, or velcro-like microstructures can be fabricated using this concept. Using the considerations in design-for-gripper-strength presented here, and combining it with design-for-gripper-functionality, new multi-purpose gripping/connecting/latching on-chip tools can be generated.

6. Summary and conclusions

The objective of this work was to develop a robust, load-bearing microgripper array and demonstrate its functionality and reliability. The gripper array system presented allows fabrication of the actuator separate from the tensile sample in order to relieve residual stresses. Gripper design considerations were first outlined. Experiments using the *simple* gripper design indicated the likelihood of gripper failure. With an improved *robust* gripper, no gripper failures were detected with $N_g = 5$ gripper pairs using post-experiment inspection both of tensile test specimens as well as specimens without a tensile bar. A statistical student *t*-test confirmed that tensile bars tested with the new gripper give rise to a greater mean strength value. The lower bound fracture force for this design is 14 mN, compared with characteristic and upper bound tensile bar fracture force of 10.6 mN and 12.2 mN, respectively. Confocal Raman microscopy was used to directly validate the FEA-calculated stresses in the grippers. The maximum stresses in the robust female grippers are ≈50% of the threshold strength.

References

[1] Monkman G J, Hesse S, Steinmann R and Schunk H 2007 *Robot Grippers* (New York: Wiley)
[2] Kim C-J, Pisano A P and Muller R S 1992 Silicon-processed overhanging microgripper *J. Microelectromech. Syst.* **1** 31–6
[3] Carrozza M C, Eisinberg A, Menciassi A, Campolo D, Micera S and Dario P 2000 Towards a force-controlled microgripper for assembling biomedical microdevices *J. Micromech. Microeng.* **10** 271
[4] Dechev N, Cleghorn W L and Mills J K 2004 Microassembly of 3D microstructures using a compliant, passive microgripper *J. Microelectromech. Syst.* **13** 176–89
[5] Kim D-H, Kim B and Kang H 2004 Development of a piezoelectric polymer-based sensorized microgripper for microassembly and micromanipulation *Microsyst. Technol.* **10** 275–80
[6] Mølhave K and Hansen O 2005 Electro-thermally actuated microgrippers with integrated force-feedback *J. Micromech. Microeng.* **15** 1265
[7] Lu Y-W and Kim C-J C 2006 Microhand for biological applications *Appl. Phys. Lett.* **89** 164101

[8] Kim K, Liu X, Zhang Y and Sun Y 2008 Nanonewton force-controlled manipulation of biological cells using a monolithic MEMS microgripper with two-axis force feedback *J. Micromech. Microeng.* **18** 055013

[9] Zhang Y, Chen B K, Liu X and Sun Y 2010 Autonomous robotic pick-and-place of microobjects *IEEE Trans. Robot.* **26** 200–7

[10] Chen B K, Zhang Y, Perovic D D and Sun Y 2011 MEMS microgrippers with thin gripping tips *J. Micromech. Microeng.* **21** 105004

[11] Malachowski K, Breger J, Kwag H R, Wang M O, Fisher J P, Selaru F M and Gracias D H 2014 Stimuli-responsive theragrippers for chemomechanical controlled release *Angew. Chem. Int. Edn.* **53** 8045–9

[12] Beyeler F, Neild A, Oberti S, Bell D J, Sun Y, Dual J and Nelson B J 2007 Monolithically fabricated microgripper with integrated force sensor for manipulating microobjects and biological cells aligned in an ultrasonic field *J. Microelectromech. Syst.* **16** 7–15

[13] Solano B and Wood D 2007 Design and testing of a polymeric microgripper for cell manipulation *Microelectron. Eng.* **84** 1219–22

[14] Ivanova K, Ivanov T, Badar A, Volland B E, Rangelow I W, Andrijasevic D, Sümecz F, Fischer S, Spitzbart M and Brenner W 2006 Thermally driven microgripper as a tool for micro assembly *Microelectron. Eng.* **83** 1393–5

[15] Volland B, Heerlein H and Rangelow I 2002 Electrostatically driven microgripper *Microelectron. Eng.* **61** 1015–23

[16] Vasudev A and Zhe J 2008 A capillary microgripper based on electrowetting *Appl. Phys. Lett.* **93** 103503

[17] Luo J K, Flewitt A J, Spearing S M, Fleck N A and Milne W I 2005 Comparison of microtweezers based on three lateral thermal actuator configurations *J. Micromech. Microeng.* **1 5** 1294

[18] Choi H-S, Lee D-C, Kim S-S and Han C-S 2005 The development of a microgripper with a perturbation-based configuration design method *J. Micromech. Microeng.* **15** 1327

[19] Kim D-H, Lee M G, Kim B and Sun Y 2005 A superelastic alloy microgripper with embedded electromagnetic actuators and piezoelectric force sensors: a numerical and experimental study *Smart Mater. Struct.* **14** 1265

[20] Chasiotis I, Cho S and Jonnalagadda K 2006 Fracture toughness and subcritical crack growth in polycrystalline silicon *J. Appl. Mech.* **73** 714–22

[21] Hazra S S, Baker M S, Beuth J L and de Boer M P 2011 Compact on-chip microtensile tester with prehensile grip mechanism *J. Microelectromech. Syst.* **20** 1043–53

[22] Saleh M E, Beuth J L and Boer M P 2014 Validated prediction of the strength size effect in polycrystalline silicon using the three-parameter Weibull function *J. Am. Ceram. Soc.* **97** 3982–90

[23] Baker M S, Plass R A, Headley T J and Walraven J A 2004 Compliant thermo-mechanical MEMS actuators *Technical Report* SAND2004-6635 (Sandia National Laboratories, Albuquerque, NM) (www.mems.sandia.gov/tech-info/doc/thermal_actuator_sand.pdf)

[24] Wittwer J W, Baker M S and Howell L L 2006 Simulation, measurement, and asymmetric buckling of thermal microactuators *Sensors Actuators A* **128** 395–401

[25] Freund L B and Suresh S 2004 *Thin Film Materials: Stress, Defect Formation and Surface Evolution* (Cambridge: Cambridge University Press)

[26] Hazra S S, Baker M S, Beuth J L and de Boer M P 2009 Demonstration of an *in situ* on-chip tensile tester *J. Micromech. Microeng.* **19** 082001

[27] Reedy E D Jr, Boyce B L, Foulk J W III, Field R V Jr, Ohlhausen J A, Hazra S S and de Boer M P 2011 Predicting fracture in micron-scale polycrystalline silicon MEMS structures *J. Microelectromech. Syst.* **20** 1043–53

[28] Sharpe W N, Yuan B and Edwards R L 1997 A new technique for measuring the mechanical properties of thin-films *J. Microelectromech. Syst.* **6** 193

[29] Greek S, Ericson F, Johansson S, Furtsch M and Rump A 1999 Mechanical characterization of thick polysilicon films: Young's modulus and fracture strength evaluated with microstructures *J. Micromech. Microeng.* **9** 245–51

[30] Jensen B D, de Boer M P, Masters N D, Bitsie F and LaVan D A 2001 Interferometry of actuated cantilevers to determine material properties and test structure non-idealities in MEMS *J. Microelectromech. Syst.* **10** 336–46

[31] Sniegowski J J and de Boer M P 2000 IC-compatible polysilicon surface micromachining *Annu. Rev. Mater. Sci.* **30** 299–333

[32] Hazra S S 2010 High throughput, on-chip, *in-situ* investigations of structural propoerties of polycrystalline silicon for microelectromechanical systems *PhD Thesis* Mechanical Engineering, Carnegie Mellon University, Pittsburgh, PA

[33] Millet O, Bernardoni P, Régnier S, Bidaud P, Tsitsiris E, Collard D and Buchaillot L 2004 Electrostatic actuated micro gripper using an amplification mechanism *Sensors Actuators A* **114** 371–8

[34] Tsuchiya T, Tabata O, Sakata J and Taga Y 1998 Specimen size effect of tensile strength of surface-micromachined polycrystalline silicon thin films *J. Microelectromech. Syst.* **7** 106–13

[35] Boyce B 2010 A sequential tensile method for rapid characterization of extreme-value behavior in microfabricated materials *Exp. Mech.* **50** 993–7

[36] Piley W 1997 *Peterson's Stress Concentration Factors* (New York: Wiley)

[37] Myers G A, Hazra S S, de Boer M P, Michaels C A, Stranick S J, Koseski R P, Cook R F and DelRio F W 2014 Stress mapping of micromachined polycrystalline silicon devices via confocal Raman microscopy *Appl. Phys. Lett.* **104** 191908

[38] Kim S H, Asay D B and Dugger M T 2007 Nanotribology and MEMS *Nano Today* **2** 22–9